

FlowComposer: Composable Flows for Compositional Zero-Shot Learning

Zhenqi He Lin Li Long Chen*

The Hong Kong University of Science and Technology

zheci@connect.ust.hk {lllidy, longchen}@ust.hk

<https://hkust-longgroup.github.io/FlowComposer/>

Abstract

Compositional zero-shot learning (CZSL) aims to recognize unseen attribute-object compositions by recombining primitives learned from seen pairs. Recent CZSL methods built on vision-language models (VLMs) typically adopt parameter-efficient fine-tuning (PEFT). They apply visual disentanglers for decomposition and manipulate token-level prompts or prefixes to encode compositions. However, such PEFT-based designs suffer from two fundamental limitations: (1) *Implicit Composition Construction*, where composition is realized only via token concatenation or branch-wise prompt tuning rather than an explicit operation in the embedding space; (2) *Remained Feature Entanglement*, where imperfect disentanglement leaves attribute, object, and composition features mutually contaminated. Together, these issues limit the generalization ability of current CZSL models. In this paper, we are the first to systematically study flow matching for CZSL and introduce *FlowComposer*, a model-agnostic framework that learns two primitive flows to transport visual features toward attribute and object text embeddings, and a learnable *Composer* that explicitly fuses their velocity fields into a composition flow. To exploit the inevitable residual entanglement, we further devise a leakage-guided augmentation scheme that reuses leaked features as auxiliary signals. We thoroughly evaluate *FlowComposer* on three public CZSL benchmarks by integrating it as a plug-and-play component into various baselines, consistently achieving significant improvements.

1. Introduction

Humans exploit *compositionality* and *decompositionality*: we learn concepts by decomposing them into a set of primitives (*i.e.*, attributes and objects) and recognize new concepts by recombining those primitives (*e.g.*, from *red apple* and *green banana* to *green apple* as shown in Fig. 1a). Moti-

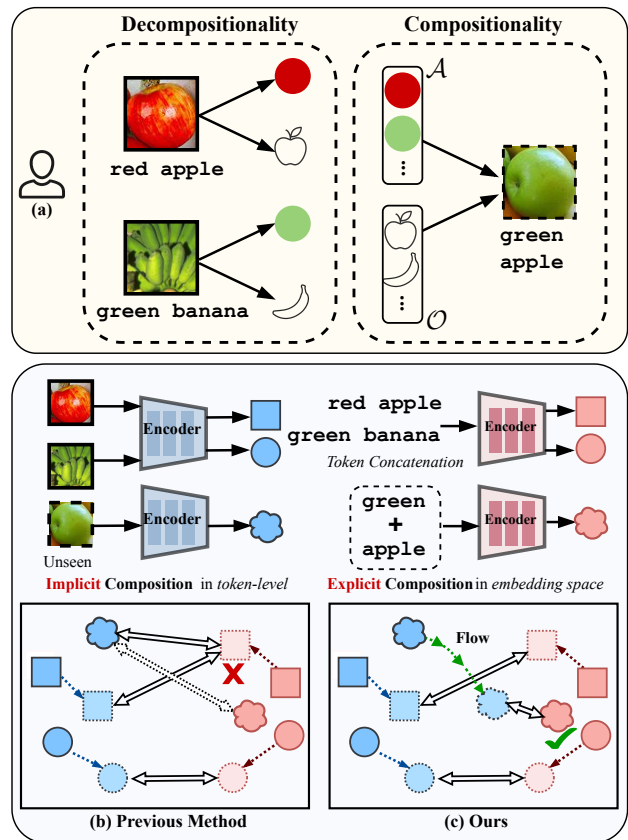


Figure 1. (a) Humans recognize new concepts by recombining familiar primitives. (b) Prior CZSL methods compose only at the token level, which may not yield valid unseen compositions in the embedding space. (c) We perform explicit composition in the embedding space via learned attribute and object flows.

vated by this, compositional zero-shot learning (CZSL) [37, 40] is proposed to train on seen attribute-object compositions and test on unseen pairs formed from the same primitives. The core objective is therefore twofold: (i) Effectively learning decomposed primitive concepts from given images and (ii) Recombining learned primitives into the composition representation for generalization.

*Corresponding author.

Recent CZSL approaches build on powerful vision-language models (VLMs) like CLIP [45], capitalizing on their aligned visual-textual spaces pre-trained on large-scale image-text pairs. In general, they measure the similarities between the query image and the text embedding of each primitive concept for zero-shot recognition. To better leverage the compositional nature, recent efforts combine both decomposed and composed strategies, powered by parameter-efficient fine-tuning (PEFT), *e.g.*, text prompt tuning and visual adapter. *On the decomposition side*, two visual disentangled are employed to independently extract visual features for attributes and objects [15, 36]. These features are then used to compute classification logits against their respective primitive text embeddings. *On the composition side*, compositional semantics are captured by constructing token-level text prompts to bind attributes and objects, and align the encoded text features with their corresponding image features. For instance, CSP [41] concatenates learnable [attribute] and [object] tokens within one prompt with fixed prefix (a photo of), while [15, 36] extend with branch-specific soft prefixes, implicitly modeling different semantic roles at the token level.

However, these PEFT-based decomposition-composition strategies suffer from two fundamental flaws: 1) **Implicit Composition Construction**: The composition relies on *token-level* concatenation rather than an explicit operation in the embedding space, so for unseen pairs the resulting composition embedding may not lie close to the corresponding image embedding, as illustrated in Fig. 1b, which in turn hampers generalization to unseen compositions. 2) **Remained Feature Entanglement**: The visual disentangler fails to enforce strict feature separation for primitives, resulting in visual streams leaking information across primitives. Such residual entanglement weakens branch-specific alignment and makes recomposed embeddings for unseen attribute-object pairs less reliable. Taken together, these flaws make PEFT-based CZSL methods prone to overfitting, and struggle to achieve a stable trade-off between seen and unseen recognition ability. As shown in Fig. 2a (left), as training progresses, the seen accuracy rises, whereas the unseen accuracy steadily drops, exposing a strong bias toward seen compositions.

Inspired by the recent success of Flow Matching (FM) where time-conditioned velocity models robustly transport latents across spaces for image generation [1, 11, 30–32], we explore flow matching as a natural computational mechanism for CZSL. The core insight is that FM’s velocity fields naturally admit combination and decomposition, aligning naturally with the essence of compositionality and decompositionality in CZSL. Guided by this view, we propose *FlowComposer*, a flow-based CZSL framework that first learns two primitive flows to transport visual features toward their corresponding text embeddings, and then ex-

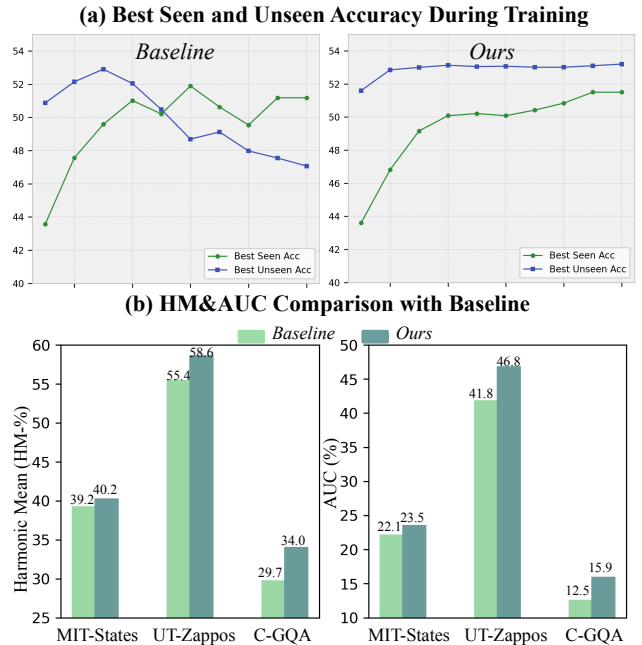


Figure 2. Training dynamics and performance comparison with baseline - Troika [15]. Our method yields a more balanced seen/unseen accuracy trajectory and consistently improves HM and AUC over the baseline on all three datasets.

PLICITLY composes these primitive velocity fields to form composition flows in the shared embedding space, as illustrated in Fig. 1c.

To address the *implicit composition construction*, we introduce an explicit **Composer** in the embedding space that combines primitive velocities into a composition velocity, yielding a learnable composition rule for transporting between compositional text and image embeddings from primitive embeddings. To address the *remained feature entanglement*, we introduce a **leakage-guided augmentation**: instead of treating cross-branch leakage as a failure of disentanglement, we explicitly reuse leaked features as cross-branch supervision signals (*e.g.*, attr-image \rightarrow obj-text) alongside standard within-branch supervision, thereby enriching velocity supervision and turning imperfect disentanglement into a source of guidance. Crucially, *FlowComposer* is model-agnostic and plug-and-play: it operates purely in the representation space, aims to tighten the distance between composed text and image embeddings, and can therefore be attached to diverse CZSL pipelines with only minor modifications. We adapt our framework to popular CZSL baselines, CSP [41] and Troika [15], leading to higher HM and AUC and a more stable balance between seen and unseen compositions, as shown in Fig. 2, where *FlowComposer* reduces the seen-unseen bias and improves overall performance across all datasets.

In summary, we make the following contributions in this paper: (i) We take an initial step towards exploiting flow

matching for CZSL, and propose *FlowComposer*, a general framework that employs composable flows atop existing CZSL pipelines to encode explicit composition operations. (ii) We introduce a leakage-guided augmentation that leverages the inherent imperfect disentanglement of attribute and object features, converting cross-branch leakage into constructive supervision to boost composition recognition. (iii) Extensive experiments on public CZSL datasets show that plugging *FlowComposer* into diverse CZSL pipelines consistently improves performance.

2. Related Work

Compositional Zero-Shot Learning (CZSL). CZSL seeks to recognize *unseen* attribute–object compositions by leveraging supervision from *seen* compositions and recombining primitive concepts learned from labels of the form (attribute, object). Early approaches fall into two broad lines. The first learns a single classifier or shared embedding that maps images and compositions into a common space for direct composition prediction, typically enforcing relations between primitives and compositions [29, 34, 38–40]. The second decouples attribute and object modeling with parallel heads, then fuses the two streams for composition recognition via late fusion [10, 20, 21, 43, 46, 51].

With the rise of powerful vision–language models (VLMs) [45], CZSL methods increasingly adopt prompt-based paradigms that exploit pre-trained alignment between images and text [15, 36, 41, 54]. CSP [41] uses a *single-path* design that represents the whole composition as one learnable prompt token and aligns this single branch with image features. In contrast, later methods [15, 25, 36, 54] adopt a *multi-path* formulation that splits the text stream into attribute and object branches with branch-specific prompts, aligns each branch to visual features, and then fuses the branches for prediction. Recent work goes further by using large language models (LLMs) to *generate additional textual knowledge* that improves compositional reasoning. For example, PLID [2] prompts LLMs to generate diverse, informative class descriptions to form language-informed text distributions, LOGICZSL [50] converts LLM-derived relational knowledge into differentiable logic rules as auxiliary losses, and PLO-LLM [24] uses LLMs to craft composition-specific graduated descriptions that guide progressive, step-wise observation.

Flow Matching (FM). FM has recently emerged as a leading paradigm for image generation. It learns a time-conditioned velocity field (neural ODE) that transports samples along a prescribed probability path from an easy prior to the data distribution by directly regressing the target velocity [1, 30, 32]. Early work [6, 8] applies this transport from noise priors to images, yielding high-fidelity synthesis comparable to diffusion [13] but with simpler dynam-

ics. More recently, text-to-image FMs [11, 31] learn cross-modal flows that carry text embeddings to image embeddings, enabling direct transportation between language and vision via learned velocities. Beyond text-to-image generation, FM has been extended to image-level transfers, *e.g.*, depth estimation [9] and semantic segmentation [3, 49].

Generative Models for Classification. Beyond synthesis, modern generative models have been widely adopted across visual perception and classification [4, 5, 23, 33, 44, 47, 48]. A large thread uses generative models to augment scarce data by synthesizing faithful and diverse samples that expand training sets for fine-grained classification [7, 16], few-shot [47], long-tailed [22], and category discovery [33]. A complementary line treats the generator itself as a classifier, converting text-to-image diffusion models into zero-shot and few-shot generative classifiers by scoring class-conditional denoising (a “diffusion classifier”) [4, 5, 23] and improving efficiency with hierarchical prompting [42] and additional image encoder [44]. Recent work also parameterizes few-shot learners via diffusion time-steps to isolate nuanced class attributes [53], and optimizes the matching noise to stabilize the pipeline [48].

While the above approaches all leverage pretrained text-to-image generators, they primarily use them either for data synthesis or by repurposing the generator as a classifier. In contrast, we exploit the core principle of distribution transportation and utilize the compositionality of velocity fields. Notably, two concurrent works [19, 26] apply flow matching for few-shot cross-modal alignment, but they do not exploit the compositional capacity of velocity fields.

3. Preliminary

In this section, we first elaborate on the CZSL task in Sec 3.1, offer a review of baselines in Sec 3.2, and introduce the flow matching mechanism in Sec 3.3.

3.1. Problem Statement

CZSL aims to recognize unseen attribute–object compositions by composing primitive concepts learned from seen compositions. Consider an attribute set $\mathcal{A} = \{a_1, \dots, a_M\}$ and an object set $\mathcal{O} = \{o_1, \dots, o_N\}$, the universe of compositional classes is the Cartesian product $\mathcal{C} = \mathcal{A} \times \mathcal{O}$, where each class $c = (a, o)$. \mathcal{C} is partitioned into disjoint seen and unseen subsets, \mathcal{C}_s and \mathcal{C}_u , with $\mathcal{C}_s \cap \mathcal{C}_u = \emptyset$. The training set is $\mathcal{D}_{\text{tr}} = \{(I_i, c_i) \mid I_i \in \mathcal{I}, c_i \in \mathcal{C}_s\}$, where \mathcal{I} denotes the image domain. At test time, the model predicts over a target composition space $\mathcal{C}_{\text{test}} \subseteq \mathcal{C}$ under two standard protocols: (i) **Closed-world:** $\mathcal{C}_{\text{test}} = \mathcal{C}_s \cup \mathcal{C}_u^{\text{sub}}$ for some $\mathcal{C}_u^{\text{sub}} \subseteq \mathcal{C}_u$ where $\mathcal{C}_u^{\text{sub}}$ is the unseen compositions in test data; (ii) **Open-world:** $\mathcal{C}_{\text{test}} = \mathcal{C}$ where the candidate label set is all valid compositions.

3.2. Review of CZSL Baselines

Single-path Baseline. CSP [41] formulates CZSL as a single-path alignment between the composition text embedding and the image embedding. Specifically, it freezes both CLIP encoders and optimizes only learnable text input tokens for attribute and object, which are inserted into a fixed template (“a photo of [attribute] [object]”). For each seen pair (a, o) , the predicted probability is computed by applying a softmax over temperature-scaled cosine similarities between the image feature and the prompt embedding, and the training objective is to minimize the cross-entropy with L_2 regularization on the learnable text tokens.

Multi-path Baseline. Troika [15] proposes a three-path architecture that jointly aligns branch-specific embeddings for state, object, and composition. Both CLIP encoders are kept frozen. On the vision side, it introduces a lightweight trainable adapter together with respective disentangled to extract branch-specific visual features. On the text side, it employs the same learnable primitive soft token across the primitive and composition branches, complemented by branch-specific soft prefixes for each prompt type. Given an image x and a pair (a, o) , each branch encodes its corresponding prompt and computes temperature-scaled cosine similarities to obtain $p_a(a|x)$, $p_o(o|x)$, and $p_c((a, o)|x)$. The model is trained by minimizing the sum of cross-entropy losses across the three branches. During inference, the final composition probability is computed as a calibrated score fusion $p_c + p_a \cdot p_o$.

3.3. Flow Matching for CZSL

Flow Matching [1, 30] learns a continuous transport between two distributions (e.g., a source X_0 and a target X_1) by regressing a time-dependent velocity field. Rectified flow [32] formulates a simple linear path between a sample pair $(\mathbf{x}_0 \sim X_0, \mathbf{x}_1 \sim X_1)$, which is defined as $\mathbf{x}_t = (1 - t)\mathbf{x}_0 + t\mathbf{x}_1$, where $t \in [0, 1]$. The corresponding ground-truth velocity along this path is constant: $\mathbf{v}^*(\mathbf{x}_t, t) = \mathbf{x}_1 - \mathbf{x}_0$. FM trains a neural network $\mathbf{v}_\theta(\mathbf{x}_t, t)$ to approximate this velocity field. Concretely, at each step we sample $(\mathbf{x}_0, \mathbf{x}_1)$ and draw $t \sim \mathcal{U}[0, 1]$ to construct \mathbf{x}_t , and minimize the conditional flow-matching objective:

$$\mathcal{L}_{\text{FM}}(\theta) = \mathbb{E}_{\mathbf{x}_0, \mathbf{x}_1, t} [\|\mathbf{v}_\theta(\mathbf{x}_t, t) - (\mathbf{x}_1 - \mathbf{x}_0)\|_2^2], \quad (1)$$

which is equivalent to matching the marginal velocity field in the original FM formulation [30, 32]. Once trained, samples can be transported between the two distributions by solving the ODE $\frac{d\mathbf{x}_t}{dt} = \mathbf{v}_\theta(\mathbf{x}_t, t)$ from $t = 0$ to 1 (or vice versa). In this paper, we follow the rectified flow formulation by constructing linear interpolation paths to transport primitive visual embeddings to their corresponding textual embeddings.

4. FlowComposer

As illustrated in Fig. 3, we propose *FlowComposer*, a general flow-based framework for CZSL. Our framework comprises two primitive flow models, a learnable Composer, and a leakage-guided augmentation strategy. We detail the primitive flows in Sec. 4.1, the Composer in Sec. 4.2, and the leakage-guided augmentation in Sec. 4.3.

Given an image I with label (a, o) , where a and o denote the attribute and object label respectively, we follow the mentioned CZSL baseline (e.g., CSP [41] or Troika [15]) with image encoder E_{img} and text encoder E_{text} to obtain visual features $\mathbf{x}_0^a, \mathbf{x}_0^o, \mathbf{x}_0^c$ and textual embeddings $\mathbf{x}_1^a, \mathbf{x}_1^o, \mathbf{x}_1^c$; we keep this feature extraction pipeline intact and perform all our flow and composition operations purely within this shared feature space.

4.1. Attribute and Object Flow Models

To support explicit composition, we first propose two separate rectified flow models, an *attribute flow* \mathbf{v}_{θ_a} and an *object flow* \mathbf{v}_{θ_o} , which learn how to transport visual features toward their respective attribute and object text embeddings. For each primitive branch $i \in \{a, o\}$, given the paired visual feature \mathbf{x}_0^i and text embedding \mathbf{x}_1^i , we sample a time $t \sim \mathcal{U}[0, 1]$ and construct the interpolated feature as $\mathbf{x}_t^i = (1 - t)\mathbf{x}_0^i + t\mathbf{x}_1^i$. The primitive flow model predicts a velocity $\hat{\mathbf{v}}_t^i = \mathbf{v}_{\theta_i}(\mathbf{x}_t^i, t)$, and is optimized with the flow matching MSE loss:

$$\mathcal{L}_{\text{MSE}}^i = \mathbb{E}_{\mathbf{x}_0^i, \mathbf{x}_1^i, t} [\|\hat{\mathbf{v}}_t^i - (\mathbf{x}_1^i - \mathbf{x}_0^i)\|_2^2]. \quad (2)$$

Besides the regression objective, we also encourage correct endpoint identification. We form a predicted endpoint $\hat{\mathbf{x}}_1^i = \mathbf{x}_t^i + (1 - t)\hat{\mathbf{v}}_t^i$, and compute a cross-entropy loss over the vocabulary of branch i by contrasting $\hat{\mathbf{x}}_1^i$ with all text embeddings $\{\mathbf{t}_k^i\}$ with temperature τ :

$$\mathcal{L}_{\text{CE}}^i = -\log \frac{\exp(\langle \text{norm}(\hat{\mathbf{x}}_1^i), \text{norm}(\mathbf{x}_1^i) \rangle / \tau)}{\sum_k \exp(\langle \text{norm}(\hat{\mathbf{x}}_1^i), \text{norm}(\mathbf{t}_k^i) \rangle / \tau)},$$

where $\langle \cdot, \cdot \rangle$ denotes the inner product and $\text{norm}(\cdot)$ denotes l_2 -normalization. The total loss of branch i is $\mathcal{L}_{\text{FM}}^i = \mathcal{L}_{\text{MSE}}^i + \mathcal{L}_{\text{CE}}^i$, which jointly regresses the velocity and classifies the predicted endpoint toward the correct text target.

During inference, we adopt a one-step transport scheme for efficiency. Given the primitive visual feature \mathbf{x}_0^i and the learned flow \mathbf{v}_{θ_i} , we approximate the endpoint embedding by evaluating the velocity at $t = 0$: $\hat{\mathbf{x}}_1^i = \mathbf{x}_0^i + \mathbf{v}_{\theta_i}(\mathbf{x}_0^i, 0)$, which provides a direct mapping from image features to the corresponding text space without numerical integration.

4.2. Composer

In practice, the relative contributions of attribute and object cues vary across samples. To capture such compositional relationships between attributes and objects, we introduce a learnable *Composer* to model how the primitives

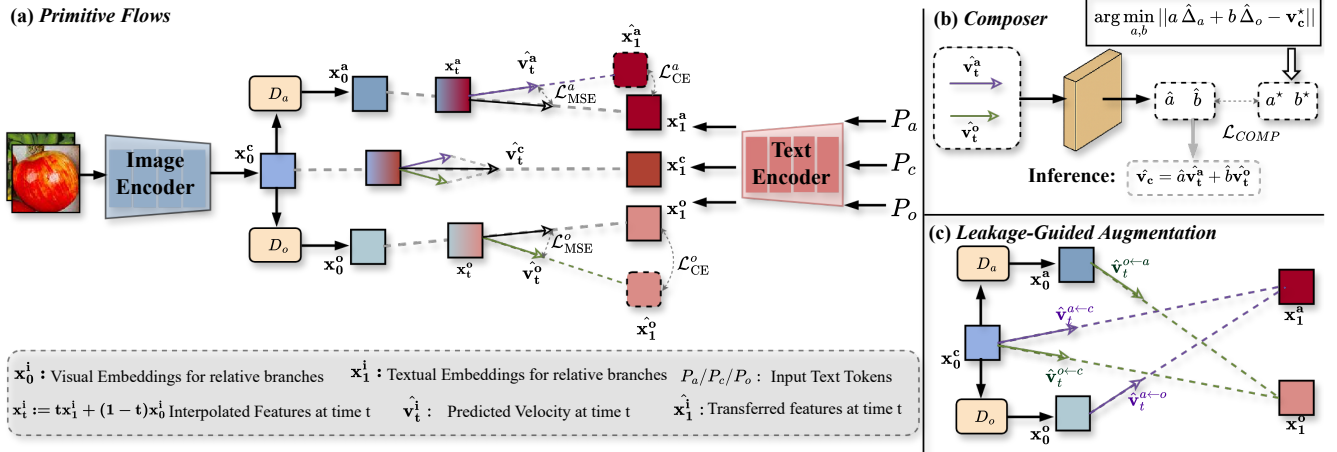


Figure 3. Overall framework for *FlowComposer*. (a) Primitive flows: Two flow models learn time-conditioned velocities to transport primitive visual embeddings to their corresponding text embeddings. (b) Composer: the network to predict the combination coefficients supervised by least-squares targets. (c) Leakage-Guided Augmentation: To exploit residual cross-branch cues, each primitive flow is also trained to transport *leaked* features from the counterpart (or composition) branch to its own text target.

combine into a composition flow in the embedding space, moving beyond token-level concatenation. For each sample, we approximate the composition velocity as a combination of primitive velocities $\mathbf{v}_c^* = a^* \mathbf{v}_a^* + b^* \mathbf{v}_o^*$, and let the Composer learn the coefficients (a^*, b^*) . For simplicity, we normalize the predicted primitive velocities to obtain unit directions $\hat{\Delta}_a = \frac{\hat{\mathbf{v}}_t^a}{\|\hat{\mathbf{v}}_t^a\|_2}$, $\hat{\Delta}_o = \frac{\hat{\mathbf{v}}_t^o}{\|\hat{\mathbf{v}}_t^o\|_2}$, and define the ground-truth composition velocity as $\mathbf{v}_c^* = \mathbf{x}_1^c - \mathbf{x}_0^c$. We then obtain target combination coefficients (a^*, b^*) by solving a least-squares problem:

$$(a^*, b^*) = \arg \min_{a,b} \|a \hat{\Delta}_a + b \hat{\Delta}_o - \mathbf{v}_c^*\|_2^2,$$

which specifies how the primitive directions should combine to approximate the composition velocity. The Composer takes the predicted normalized primitive velocities $(\hat{\mathbf{v}}_a, \hat{\mathbf{v}}_o)$ as input and outputs coefficients (\hat{a}, \hat{b}) , trained with $\mathcal{L}_{\text{comp}} = \mathbb{E} [\|\hat{a} - a^*\|_2^2 + \|\hat{b} - b^*\|_2^2]$.

At inference, we first predict the attribute $\hat{\mathbf{v}}_a$ and object velocity $\hat{\mathbf{v}}_o$ by primitive flows, and then compute the composition velocity $\hat{\mathbf{v}}_c = \hat{a} \text{norm}(\hat{\mathbf{v}}_a) + \hat{b} \text{norm}(\hat{\mathbf{v}}_o)$, and then perform a one-step update in the embedding space $\hat{\mathbf{x}}_1^c = \mathbf{x}_0^c + h \hat{\mathbf{v}}_c$, where h is a hyperparameter to control the step-size.

4.3. Leakage-guided Augmentation

As discussed above, visual disentanglers cannot enforce strict separation between primitives: each branch retains *remained feature entanglement*, where information from one primitive inevitably leaks into the other’s stream. Instead of treating this leakage as a flaw, we reinterpret it as a privileged signal via *leakage-guided augmentation*.

For each primitive branch $i \in \{a, o\}$ with target text embedding \mathbf{x}_1^i , we sample *leaked* visual features from the other streams $j \in \{a, o, c\}, j \neq i$, denoted as \mathbf{x}_0^j . Due to imperfect disentanglement, we posit that \mathbf{x}_0^j still encodes visual cues relevant to primitive i . Thus, the flow v_{θ_i} should also be able to transport these leaked visual features toward \mathbf{x}_1^i . Concretely, we sample $t \sim \mathcal{U}[0, 1]$ and construct $\mathbf{x}_t^{i \leftarrow j} = (1-t)\mathbf{x}_0^j + t\mathbf{x}_1^i$, then predict the velocity $\hat{\mathbf{v}}_t^{i \leftarrow j} = v_{\theta_i}(\mathbf{x}_t^{i \leftarrow j}, t)$. The leakage-guided flow-matching MSE loss is formulated as:

$$\mathcal{L}_{\text{MSE-leak}}^i = \mathbb{E}_{j \neq i, \mathbf{x}_0^j, \mathbf{x}_1^i, t} [\|\hat{\mathbf{v}}_t^{i \leftarrow j} - (\mathbf{x}_1^i - \mathbf{x}_0^j)\|_2^2].$$

Similarly, we also impose a contrastive endpoint constraint on the leaked paths. We define the predicted endpoint $\hat{\mathbf{x}}_1^{i \leftarrow j} = \mathbf{x}_t^{i \leftarrow j} + (1-t) \hat{\mathbf{v}}_t^{i \leftarrow j}$, and compute a cross-entropy loss over the vocabulary of branch i :

$$\mathcal{L}_{\text{CE-leak}}^i = -\log \frac{\exp(\langle \text{norm}(\hat{\mathbf{x}}_1^{i \leftarrow j}), \text{norm}(\mathbf{x}_1^i) \rangle / \tau)}{\sum_k \exp(\langle \text{norm}(\hat{\mathbf{x}}_1^{i \leftarrow j}), \text{norm}(\mathbf{t}_k^i) \rangle / \tau)},$$

where $\{\mathbf{t}_k^i\}$ are all text embeddings of branch i . The total leakage-guided loss for branch i is:

$$\mathcal{L}_{\text{leak}}^i = \mathcal{L}_{\text{MSE-leak}}^i + \mathcal{L}_{\text{CE-leak}}^i,$$

5. Experiment

5.1. Setups and Implementations

Datasets. We conduct a comprehensive evaluation of our method across three real-world CZSL benchmarks: (i) MIT-

Table 1. Quantitative comparison (§ 5.2) on three benchmarks within closed-world and open-world setting. * denotes results from our implementation. ‡ represents the methods leveraging the LLM’s knowledge.

Method	MIT-States [17]				UT-Zappos [52]				C-GQA [39]			
	Seen	Unseen	HM	AUC	Seen	Unseen	HM	AUC	Seen	Unseen	HM	AUC
<i>Closed-world Results</i>												
CLIP [45] _[ICML21]	30.2	46.0	26.1	11.0	15.8	49.1	15.6	5.0	7.5	25.0	8.6	1.4
CoOP [55] _[IJCV22]	34.4	47.6	29.8	13.5	52.1	49.3	34.6	18.8	20.5	26.8	17.1	4.4
DFSP(i2t) [36] _[CVPR23]	47.4	52.4	37.2	20.7	64.2	66.4	45.1	32.1	35.6	29.3	24.3	8.7
DFSP(BiF) [36] _[CVPR23]	47.1	52.8	37.7	20.8	63.3	69.2	47.1	33.5	36.5	32.0	26.2	9.9
DFSP(t2i) [36] _[CVPR23]	46.9	52.0	37.3	20.6	66.7	71.7	47.2	36.0	38.2	32.0	27.1	10.5
DLM [14] _[CVPR23]	46.3	49.8	37.4	20.0	67.1	72.5	52.0	39.6	32.4	28.5	21.9	7.3
CDS-CZSL [28] _[CVPR24]	50.3	52.9	39.2	22.4	63.9	74.8	52.7	39.5	38.3	34.2	28.1	11.1
IMAX[18] _[TPAMI25]	48.7	53.8	39.1	21.9	69.3	70.7	54.2	40.6	39.7	35.8	29.8	12.8
PLID [‡] [2] _[ECCV24]	49.7	52.4	39.0	22.1	67.3	68.8	52.4	38.7	38.8	33.0	27.9	11.0
PLO [‡] [24] _[ACMMM25]	51.6	53.7	40.2	23.4	70.3	75.8	55.3	43.6	44.7	38.1	33.0	14.9
LOGICZSL [‡] [50] _[CVPR25]	50.8	53.9	40.5	23.4	69.6	74.9	57.8	45.8	44.4	39.4	33.3	15.3
CSP* [41] _[ICLR23]	47.0	49.6	36.6	19.6	63.4	65.3	47.0	32.4	24.6	29.6	19.3	5.8
+FlowComposer	48.3 ^{‡3.1}	50.4 ^{‡0.8}	37.6 ^{‡1.0}	20.7 ^{‡1.1}	66.6 ^{‡3.2}	68.2 ^{‡2.9}	51.2 ^{‡4.2}	37.8 ^{‡5.4}	29.0 ^{‡4.4}	30.9 ^{‡1.3}	22.9 ^{‡3.6}	7.7 ^{‡1.9}
Troika* [15] _[CVPR24]	49.3	52.5	39.2	22.1	66.3	73.4	55.4	41.8	41.0	35.7	29.7	12.5
+FlowComposer	51.5 ^{‡2.2}	53.2 ^{‡0.7}	40.2 ^{‡1.0}	23.5 ^{‡1.4}	71.1 ^{‡4.8}	74.9 ^{‡1.5}	58.6 ^{‡3.2}	46.8 ^{‡5.0}	44.8 ^{‡3.8}	40.7 ^{‡5.0}	34.0 ^{‡4.3}	15.9 ^{‡3.4}
<i>Open-world Results</i>												
CLIP [45] _[ICML21]	30.1	14.3	12.8	3.0	15.7	20.6	11.2	2.2	7.5	4.6	4.0	0.27
CoOP [55] _[IJCV22]	34.6	9.3	12.3	2.8	52.1	31.5	28.9	13.2	21.0	4.6	5.5	0.70
DFSP(i2t) [36] _[CVPR23]	47.2	18.2	19.1	6.7	64.3	53.8	41.2	26.4	35.6	6.5	9.0	1.95
DFSP(BiF) [36] _[CVPR23]	47.1	18.1	19.2	6.7	63.5	57.2	42.7	27.6	36.4	7.6	10.6	2.39
DFSP(t2i) [36] _[CVPR23]	47.5	18.5	19.3	6.8	66.8	60.0	44.0	30.3	38.3	7.2	10.4	2.40
CDS-CZSL [28] _[CVPR24]	49.4	21.8	22.1	8.5	64.7	61.3	48.2	32.3	37.6	8.2	11.6	2.7
IMAX[18] _[TPAMI25]	50.2	18.6	21.4	7.6	68.4	57.3	47.5	32.3	38.7	7.9	11.2	2.5
PLID [‡] [2] _[ECCV24]	49.1	18.7	20.4	7.3	67.6	55.5	46.6	30.8	39.1	7.5	10.6	2.5
PLO [‡] [24] _[ACMMM25]	49.7	19.4	21.4	7.8	68.0	63.5	47.8	33.1	43.9	10.4	13.9	3.9
LOGICZSL [‡] [50] _[CVPR25]	50.7	21.4	22.4	8.7	69.6	63.7	50.8	36.2	43.7	9.3	12.6	3.4
CSP* [41] _[ICLR23]	47.4	15.3	17.1	5.6	63.4	44.8	40.6	23.3	29.6	5.4	7.3	1.3
+FlowComposer	48.2 ^{‡0.8}	15.6 ^{‡0.3}	17.8 ^{‡0.7}	6.1 ^{‡0.5}	66.4 ^{‡3.0}	46.2 ^{‡1.4}	41.2 ^{‡0.6}	25.3 ^{‡2.0}	31.2 ^{‡0.6}	5.8 ^{‡0.4}	8.0 ^{‡0.7}	1.8 ^{‡0.5}
Troika* [15] _[CVPR24]	50.3	17.5	19.0	6.8	65.8	61.0	46.6	32.7	40.8	8.6	11.7	2.9
+FlowComposer	50.4 ^{‡0.1}	19.0 ^{‡1.5}	20.3 ^{‡1.3}	7.5 ^{‡0.7}	70.1 ^{‡4.3}	61.2 ^{‡0.2}	51.0 ^{‡4.4}	35.5 ^{‡2.8}	43.5 ^{‡2.7}	10.2 ^{‡1.6}	12.6 ^{‡0.9}	3.5 ^{‡0.6}

States [17] (ii) UT-Zappos [52] (iii) C-GQA [39]. We follow the data split protocol of [41, 43] to partition datasets into train, validation, and test datasets.

Evaluation Metrics. Following the standard CZSL protocol [15, 41], we apply a calibration bias to the *unseen* scores and sweep it from $-\infty$ to $+\infty$ to balance predictions between seen and unseen compositions. Over this sweep, we report the Area Under the Curve (AUC) of the seen–unseen trade-off and the best harmonic mean (HM). For completeness, we also record the best-seen accuracy **Seen** and the best-unseen accuracy **Unseen** achieved during the sweep. For open-world evaluation, we adopt the post-training calibration strategy of [41] to discard infeasible compositions.

Implementation Details. We follow standard CZSL settings and use the pre-trained CLIP ViT-L/14 [45] as both image and text encoder. We implement *FlowComposer* on two popular CZSL baselines - CSP [41] and Troika [15]. For the single-path baseline [41], we derive attribute and

object text embeddings using simple prompts (“a photo of [attribute]” / “a photo of [object]”), and apply our primitive flows and composer accordingly. The leakage-guided augmentation is used only with the multi-path methods [15], since single-path method [41] does not provide branch-wise visual disentanglement. We employ a lightweight architecture proposed in MAR [27] as flow matching network, implemented as a deep residual MLP with timestep conditioning. For *Composer*, we employ a small three-layer MLP with LayerNorm and GELU [12] activations. Further details on datasets, optimization, and hyperparameters are deferred to the supplementary material.

5.2. Main Results

Tab. 1 reports quantitative comparisons with recent CZSL methods on three benchmarks (MIT-States [17], UT-Zappos [52] and C-GQA [39]) under both closed-world and open-world settings. Plugging our *FlowComposer* into

Table 2. Ablations. The results regarding the different components in our *FlowComposer* on MIT-States [17] and UT-Zappos [52].

	<i>Flows</i> (§ 4.1)	<i>Composer</i> (§ 4.2)	<i>LG-Aug</i> (§ 4.3)	MIT-States [17]				UT-Zappos [52]			
				Seen	Unseen	HM	AUC	Seen	Unseen	HM	AUC
Baseline	✗	✗	✗	49.3	52.5	39.2	22.1	66.3	73.4	55.4	41.8
(1)	✓	✗	✗	51.3	52.1	39.4	22.6	68.8	74.8	55.1	43.0
(2)	✓	✗	✓	51.3	53.0	40.3	23.3	69.2	74.9	56.3	44.0
(3)	✓	✓	✗	51.0	53.0	40.1	23.3	69.7	74.9	58.5	45.8
Ours	✓	✓	✓	51.5	53.2	40.2	23.5	71.1	74.9	58.6	46.8

both CSP [41] and Troika [15] consistently improve the performance in four metrics across all datasets and settings, showing that our flow-based formulation is robust and model-agnostic. In the **closed-world** setting, *FlowComposer* on Troika [15] achieves state-of-the-art AUC on all three datasets, even surpassing approaches that exploit additional LLM-generated knowledge (e.g., PLID [2], PLO [24], LOGICZSL [50]). Specifically, we improve AUC over Troika [15] by +1.4% on MIT-States, +5.0% on UT-Zappos and +3.4% on C-GQA. In the **open-world** setting, *FlowComposer* brings substantial HM and AUC gains over CSP [41] and Troika [15], e.g., +1.3% HM on MIT-States [17], +4.4% HM on UT-Zappos [52], and +0.9% on C-GQA [39] compared with Troika. The consistent improvements over baselines for all datasets and settings illustrate the effectiveness and robustness of our *FlowComposer*, and highlight flow matching as a natural and well-suited paradigm for CZSL. Although our method is slightly behind LOGICZSL [50] on AUC under the open-world setting, we note that LOGICZSL benefits from extra logic rules derived from LLMs, whereas our method attains strong generalization without using external textual knowledge.

5.3. Diagnostic Analysis

Component Analysis. We conduct ablations to quantify the contribution of each module: *Primitive Flows (Flows)*, *Composer*, and *Leakage-Guided Augmentation (LG-Aug)*. As shown in Tab. 2, we report results under the closed-world setting on MIT-States [17] and UT-Zappos [52], comparing against the Troika [15] baseline. Starting from the baseline, we incrementally integrate the proposed components. Four observations can be drawn. **First**, incorporating *primitive flows* (Row (1)) yields a modest improvement particularly on the seen compositions. **Second**, adding *Leakage-Guided Augmentation* (Row (2)) further improves alignment and robustness, leading to improvements in AUC and HM (+0.9% HM on MIT-States and +1.2% HM on UT-Zappos). **Third**, alternatively, introducing the *Composer* on top of flows (Row (3)) also stabilizes recognition, increasing both AUC and HM. **Fourth**, combining all components, the full framework achieves substantial gains over all metrics, indicating that explicit velocity composition and leakage-guided supervision are complementary to flow learning.

Primitive Flows vs. Composition Flows. To justify the

design choice of using two primitive flows, we ablate (i) a *single-flow* variant that learns one cross-modal flow directly for composition (c only), and (ii) a *three-flow* variant that adds an extra composition flow on top of the attribute/object flows ($c+a+o$) to replace the composer (see first four rows of Tab. 3). As seen, whether using a single composition flow (c) or a three-flow setup ($c+a+o$), unseen-composition accuracy degrades (around 4% deduction for MIT-States [17] and over 10% deduction for UT-Zappos [52]). We attribute this to a lack of open-world capacity: a composition flow directly models seen pair trajectories, but unseen compositions never appear in training, so the model overfits to seen pair geometry. In contrast, primitive flows learn attribute and object transports where all those attribute and object categories are seen during training; composing these transports at test time confers better generalization to unseen attribute-object combinations.

Table 3. Analysis on flows (§ 4.1) on the MIT-States [17] and UT-Zappos [52] under closed-world setting.

	MIT-States				UT-Zappos			
	S	U	H	A	S	U	H	A
<i>N/A</i>	49.3	52.5	39.2	22.1	66.3	73.4	55.4	41.8
c	50.9	48.0	36.9	20.0	70.0	60.1	44.6	37.2
$c+a+o$	51.0	48.7	37.4	20.5	70.1	60.6	44.9	37.6
<i>FlowComposer</i>	51.5	53.2	40.2	23.5	71.1	74.9	58.6	46.8

Visualization. Fig. 4 shows top-1 predictions between two baselines (CSP [41] and Troika [15]) and our *FlowComposer*. For success cases, *FlowComposer* is more reliable than baseline methods, correctly identifying compositions that the baseline misclassifies. For instance, it predicts Wood Table even when key visual cues are occluded, where Troika fails, and it further corrects both attribute and object for some cases (e.g., from Leather to Hair.Calf, from Table to Blanket, from New Tire to Clean Truck), reflecting stronger sensitivity to fine-grained primitives. For failure cases, our predictions remain semantically close to the ground truth, such as White Motorcycle for Gray Motorcycle or Blue Water for Dark Water, indicating that even when incorrect, *FlowComposer* tends to produce plausible compositions rather than irrelevant ones.

Composer vs. Predictor. To further analyze the rationale



Figure 4. Visual comparisons between CSP [41], Troika [15] and our *FlowComposer* on three datasets. Red represents the wrong prediction, and Green represents the right prediction.

of the *Composer*, we ablate it with a *direct predictor* variant that takes the same primitive velocities as inputs and with the same model structure but regresses the composition velocity outright, instead of predicting combination coefficients. We report the comparison between predictor and composer in Tab. 4 based on the Troika+*FlowComposer* setup. The predictor can be treated as a non-linear counterpart that maps primitive velocities to the composition velocity. This non-linear variant consistently underperforms our Composer (e.g., 0.2% AUC deduction in MIT-States [17], 1.6% AUC deduction in UT-Zappos [52] and 0.2% AUC deduction in C-GQA [39]), supporting the design choice of learning an explicit combination rule.

Table 4. Comparison between Predictor and Composer in MIT-States [17], UT-Zappos [52] and C-GQA [39] on HM and AUC under the closed-world setting.

	MIT-States		UT-Zappos		C-GQA	
	HM	AUC	HM	AUC	HM	AUC
Predictor	39.9	23.3	58.6	45.2	33.9	15.7
Composer	40.2	23.5	58.6	46.8	34.0	15.9

FM vs Regressor. To verify that our improvements stem from the *flow-matching formulation* rather than extra parameters, we add a parameter-matched regressor baseline. Concretely, we reuse the *same* network architecture as our velocity model, but use it to predict an endpoint residual in feature space: $\hat{x}_1^i = x_0^i + \Delta_\phi(x_0^i)$, where Δ_ϕ is trained to minimize a classification loss against the target text embedding. This removes the time-conditioning and velocity supervision, keeping total trainable parameters and FLOPs comparable to our FM branch. As reported in Tab. 5, the parameter-matched regressor lags behind our flow matching based approach across all three datasets and metrics, despite equal capacity and similar inference cost. These results indicate that the gain comes from our design of us-

ing flow matching, not from adding parameters or larger adapters. Taken together, this comparison suggests that time-conditioned velocity supervision is inherently more suitable for capturing composition dynamics than merely attaching a residual regression head, even when the number of trainable parameters is matched.

Table 5. Comparison between regressor and our *FM* on HM and AUC under the closed-world setting.

	MIT-States		UT-Zappos		C-GQA	
	HM	AUC	HM	AUC	HM	AUC
Regressor	39.6	22.5	55.2	42.8	30.0	12.9
FM	40.2	23.5	58.6	46.8	34.0	15.9

6. Conclusion

In this paper, we take a first step towards leveraging flow matching for compositional zero-shot learning, motivated by the natural compositionality and decompositionality of velocity fields in the embedding space. *First*, we introduce *FlowComposer*, a general framework that learns attribute and object flows and explicitly composes them via a learnable Composer, replacing implicit *token-level* concatenation with an operational composition rule in the embedding space. *Second*, we propose a leakage-guided augmentation strategy that converts cross-branch leakage into useful supervisory signals to further exploit inevitable residual entanglement in existing CZSL pipelines. *Third*, we conduct extensive experiments on three public CZSL benchmarks and two strong VLM-based baselines which demonstrate that *FlowComposer* consistently improves HM and AUC, yields a more balanced trade-off between seen and unseen performance, and incurs only negligible inference overhead, further supporting flow matching as a natural and effective paradigm for CZSL.

Acknowledgments. This work was supported by the National Natural Science Foundation of China Young Scholar Fund Category C (62402408), the Hong Kong SAR RGC Early Career Scheme (26208924), the National Natural Science Foundation of China Young Scholar Fund Category B (62522216), and the Hong Kong SAR RGC General Research Fund (16219025). Thanks to Yanghao Wang for GPU support.

References

- [1] Michael Samuel Albergo and Eric Vanden-Eijnden. Building normalizing flows with stochastic interpolants. In *ICLR*, 2023. 2, 3, 4
- [2] Wentao Bao, Lichang Chen, Heng Huang, and Yu Kong. Prompting language-informed distribution for compositional zero-shot learning. In *ECCV*, 2024. 3, 6, 7
- [3] Lea Bogensperger, Dominik Narnhofer, Alexander Falk, Konrad Schindler, and Thomas Pock. Flowsdf: Flow matching for medical image segmentation using distance transforms. *IJCV*, 2025. 3
- [4] Huanran Chen, Yinpeng Dong, Zhengyi Wang, Xiao Yang, Chengqi Duan, Hang Su, and Jun Zhu. Robust classification via a single diffusion model. *arXiv preprint arXiv:2305.15241*, 2023. 3
- [5] Kevin Clark and Priyank Jaini. Text-to-image diffusion models are zero shot classifiers. In *NeurIPS*, 2023. 3
- [6] Patrick Esser, Sumith Kulal, Andreas Blattmann, Rahim Entezari, Jonas Müller, Harry Saini, Yam Levi, Dominik Lorenz, Axel Sauer, Frederic Boesel, et al. Scaling rectified flow transformers for high-resolution image synthesis. In *ICML*, 2024. 3
- [7] Yunxiang Fu, Chaoqi Chen, Yu Qiao, and Yizhou Yu. Dreamda: Generative data augmentation with diffusion models. *arXiv preprint arXiv:2403.12803*, 2024. 3
- [8] Zhengyang Geng, Mingyang Deng, Xingjian Bai, J Zico Kolter, and Kaiming He. Mean flows for one-step generative modeling. In *NeurIPS*, 2025. 3
- [9] Ming Gui, Johannes Schusterbauer, Ulrich Prestel, Pingchuan Ma, Dmytro Kotoenko, Olga Grebenkova, Stefan Andreas Baumann, Vincent Tao Hu, and Björn Ommer. Depthfm: Fast generative monocular depth estimation with flow matching. In *AAAI*, 2025. 3
- [10] Shaozhe Hao, Kai Han, and Kwan-Yee K Wong. Learning attention as disentangler for compositional zero-shot learning. In *CVPR*, 2023. 3
- [11] Ju He, Qihang Yu, Qihao Liu, and Liang-Chieh Chen. Flowtok: Flowing seamlessly across text and image tokens. In *ICCV*, 2025. 2, 3
- [12] Dan Hendrycks and Kevin Gimpel. Gaussian error linear units (gelus). *arXiv preprint 1606.08415*, 2016. 6
- [13] Jonathan Ho, Ajay Jain, and Pieter Abbeel. Denoising diffusion probabilistic models. *NeurIPS*, 2020. 3
- [14] Xiaoming Hu and Zilei Wang. A dynamic learning method towards realistic compositional zero-shot learning. In *AAAI*, 2024. 6
- [15] Siteng Huang, Biao Gong, Yutong Feng, Min Zhang, Yiliang Lv, and Donglin Wang. Troika: Multi-path cross-modal traction for compositional zero-shot learning. In *CVPR*, 2024. 2, 3, 4, 6, 7, 8, 11, 12, 13, 14
- [16] Khawar Islam, Muhammad Zaigham Zaheer, Arif Mahmood, and Karthik Nandakumar. Diffusemix: Label-preserving data augmentation with diffusion models. In *CVPR*, 2024. 3
- [17] Phillip Isola, Joseph J Lim, and Edward H Adelson. Discovering states and transformations in image collections. In *CVPR*, 2015. 6, 7, 8, 11, 12, 13, 14
- [18] Chenyi Jiang, Shidong Wang, Yang Long, Zechao Li, Haofeng Zhang, and Ling Shao. Imaginary-connected embedding in complex space for unseen attribute-object discrimination. *IEEE TPAMI*, 2025. 6
- [19] Ziqi Jiang, Yanghao Wang, and Long Chen. Exploring cross-modal flows for few-shot learning. *arXiv preprint arXiv:2510.14543*, 2025. 3
- [20] Shyamgopal Karthik, Massimiliano Mancini, and Zeynep Akata. Kg-sp: Knowledge guided simple primitives for open world compositional zero-shot learning. In *CVPR*, 2022. 3
- [21] Hanjae Kim, Jiyoung Lee, Seongheon Park, and Kwanghoon Sohn. Hierarchical visual primitive experts for compositional zero-shot learning. In *ICCV*, 2023. 3
- [22] GaYeon Koh, Hyun-Jic Oh, Jeonghyun Noh, and Won-Ki Jeong. Synthetic data augmentation using pre-trained diffusion models for long-tailed food image classification. In *CVPR Workshop*, 2025. 3
- [23] Alexander C Li, Mihir Prabhudesai, Shivam Duggal, Ellis Brown, and Deepak Pathak. Your diffusion model is secretly a zero-shot classifier. In *ICCV*, 2023. 3
- [24] Lin Li, Guikun Chen, Jun Xiao, and Long Chen. Compositional zero-shot learning via progressive language-based observations. In *ACM MM*, 2025. 3, 6, 7
- [25] Lin Li, Jiahui Li, Jiaming Lei, Jun Xiao, Feifei Shao, and Long Chen. H²em: Learning hierarchical hyperbolic embeddings for compositional zero-shot learning. *arXiv preprint arXiv: 2512.20029*, 2025. 3
- [26] Lin Li, Ziqi Jiang, Gefan Ye, Zhenqi He, Jiahui Li, Jun Xiao, Kwang-Ting Cheng, and Long Chen. Path-decoupled hyperbolic flow matching for few-shot adaptation. *arXiv preprint arXiv:2602.20479*, 2026. 3
- [27] Tianhong Li, Yonglong Tian, He Li, Mingyang Deng, and Kaiming He. Autoregressive image generation without vector quantization. In *NeurIPS*, 2024. 6, 11
- [28] Yun Li, Zhe Liu, Hang Chen, and Lina Yao. Context-based and diversity-driven specificity in compositional zero-shot learning. In *CVPR*, 2024. 6
- [29] Yong-Lu Li, Yue Xu, Xiaohan Mao, and Cewu Lu. Symmetry and group in attribute-object compositions. In *CVPR*, 2020. 3
- [30] Yaron Lipman, Ricky T. Q. Chen, Heli Ben-Hamu, Maximilian Nickel, and Matthew Le. Flow matching for generative modeling. In *ICLR*, 2023. 2, 3, 4
- [31] Qihao Liu, Xi Yin, Alan Yuille, Andrew Brown, and Mannat Singh. Flowing from words to pixels: A noise-free framework for cross-modality evolution. In *CVPR*, 2025. 3

- [32] Xingchao Liu, Chengyue Gong, and Qiang Liu. Flow straight and fast: Learning to generate and transfer data with rectified flow. In *ICLR*, 2023. 2, 3, 4
- [33] Xiao Liu, Nan Pu, Haiyang Zheng, Wenjing Li, Nicu Sebe, and Zhun Zhong. Generate, refine, and encode: Leveraging synthesized novel samples for on-the-fly fine-grained category discovery. In *ICCV*, 2025. 3
- [34] Zhe Liu, Yun Li, Lina Yao, Xiaojun Chang, Wei Fang, Xiaojun Wu, and Abdulmoteleb El Saddik. Simple primitives with feasibility- and contextuality-dependence for open-world compositional zero-shot learning. *IEEE TPAMI*, 2023. 3
- [35] Ilya Loshchilov and Frank Hutter. Decoupled weight decay regularization. In *ICLR*, 2019. 11
- [36] Xiaocheng Lu, Song Guo, Ziming Liu, and Jingcai Guo. Decomposed soft prompt guided fusion enhancing for compositional zero-shot learning. In *CVPR*, 2023. 2, 3, 6
- [37] Massimiliano Mancini, Muhammad Ferjad Naeem, Yongqin Xian, and Zeynep Akata. Open world compositional zero-shot learning. In *CVPR*, 2021. 1
- [38] Ishan Misra, Abhinav Gupta, and Martial Hebert. From red wine to red tomato: Composition with context. In *CVPR*, 2017. 3
- [39] Muhammad Ferjad Naeem, Yongqin Xian, Federico Tombari, and Zeynep Akata. Learning graph embeddings for compositional zero-shot learning. In *CVPR*, 2021. 6, 7, 8, 11, 12, 13, 14
- [40] Tushar Nagarajan and Kristen Grauman. Attributes as operators: factorizing unseen attribute-object compositions. In *ECCV*, 2018. 1, 3
- [41] Nihal V Nayak, Peilin Yu, and Stephen Bach. Learning to compose soft prompts for compositional zero-shot learning. In *ICLR*, 2023. 2, 3, 4, 6, 7, 8, 11, 12, 13, 14
- [42] Wenxin Ning, Dongliang Chang, Yujun Tong, Zhongjiang He, Kongming Liang, and Zhanyu Ma. Hierarchical prompting for diffusion classifiers. In *ACCV*, 2024. 3
- [43] Senthil Purushwalkam, Maximilian Nickel, Abhinav Gupta, and Marc’Aurelio Ranzato. Task-driven modular networks for zero-shot compositional learning. In *CVPR*, 2019. 3, 6, 11
- [44] Zipeng Qi, Buhua Liu, Shiyang Zhang, Bao Li, Zhiqiang Xu, Haoyi Xiong, and Zeke Xie. A simple and efficient baseline for zero-shot generative classification. *arXiv preprint arXiv:2412.12594*, 2024. 3
- [45] Alec Radford, Jong Wook Kim, Chris Hallacy, Aditya Ramesh, Gabriel Goh, Sandhini Agarwal, Girish Sastry, Amanda Askell, Pamela Mishkin, Jack Clark, et al. Learning transferable visual models from natural language supervision. In *ICML*, 2021. 2, 3, 6, 11
- [46] Qingsheng Wang, Lingqiao Liu, Chenchen Jing, Hao Chen, Guoqiang Liang, Peng Wang, and Chunhua Shen. Learning conditional attributes for compositional zero-shot learning. In *CVPR*, 2023. 3
- [47] Yanghao Wang and Long Chen. Inversion circle interpolation: Diffusion-based image augmentation for data-scarce classification. In *CVPR*, 2025. 3
- [48] Yanghao Wang and Long Chen. Noise matters: Optimizing matching noise for diffusion classifiers. In *NeurIPS*, 2025. 3
- [49] Zanyi Wang, Dengyang Jiang, Liuzhuozheng Li, Sizhe Dang, Chengzu Li, Harry Yang, Guang Dai, Mengmeng Wang, and Jingdong Wang. Deforming videos to masks: Flow matching for referring video segmentation. *arXiv preprint arXiv:2510.06139*, 2025. 3
- [50] Peng Wu, Xiankai Lu, Hao Hu, Yongqin Xian, Jianbing Shen, and Wenguan Wang. Logiczsl: Exploring logic-induced representation for compositional zero-shot learning. In *CVPR*, 2025. 3, 6, 7
- [51] Muli Yang, Cheng Deng, Junchi Yan, Xianglong Liu, and Dacheng Tao. Learning unseen concepts via hierarchical decomposition and composition. In *CVPR*, 2020. 3
- [52] Aron Yu and Kristen Grauman. Fine-grained visual comparisons with local learning. In *CVPR*, 2014. 6, 7, 8, 11, 12, 13, 14
- [53] Zhongqi Yue, Pan Zhou, Richang Hong, Hanwang Zhang, and Qianru Sun. Few-shot learner parameterization by diffusion time-steps. In *CVPR*, 2024. 3
- [54] Shiyu Zhang, Cheng Yan, Yang Liu, Chenchen Jing, Lei Zhou, and Wenjun Wang. Learning visual proxy for compositional zero-shot learning. In *ICCV*, 2025. 3
- [55] Kaiyang Zhou, Jingkang Yang, Chen Change Loy, and Ziwei Liu. Learning to prompt for vision-language models. *IJCV*, 2022. 6

FlowComposer: Composable Flows for Compositional Zero-Shot Learning

Supplementary Material

We provide additional details and experimental results in this supplementary material, which is organized as follows:

- §7 More Experimental Details
- §8 Remained Feature Entanglement Analysis
- §9 Additional Analysis
- §10 Stability Analysis
- §11 Semantic Analysis of Composer
- §12 Social Impacts

7. More Experimental Details

7.1. Dataset Statistics

For each dataset, we adhere to the data splitting scheme from [41, 43]. Detailed data statistics are reported in Tab. 6. MIT-States [17] is a large-scale attribute–object benchmark containing diverse everyday objects paired with a wide range of state attributes (e.g., *sliced*, *moldy*, *wet*), resulting in a dense and visually heterogeneous composition space. UT-Zappos [52] focuses on fine-grained footwear recognition, where attributes primarily describe material or surface appearance (e.g., *leather*, *satın*, *suede*) and objects correspond to specific shoe categories. C-GQA [39] extends the GQA dataset with compositional attribute–object annotations, covering a much broader variety of scenes, colors, textures, and object types, and thus presents a more diverse and challenging open-world composition landscape.

Table 6. Statistics of three datasets in our experiments. The number of elements in each set is reported.

Dataset	S		Training				Validation			Test		
	S	O	C ^{sc}	X	C ^{sc}	C ^{us}	X	C ^{sc}	C ^{us}	X		
MIT-States [17]	115	245	1262	30k	300	300	10k	400	400	13k		
UT-Zappos [52]	16	12	83	23k	15	15	3k	18	18	3k		
C-GQA [39]	413	674	5592	27k	1252	1040	7k	888	923	5k		

7.2. Additional Implementation Details

Consistent with prior studies [15, 41], we adopt the official OpenAI checkpoints of CLIP with a ViT-L/14 [45] configuration as our visual–textual backbone. For data preprocessing and training configuration, we follow the same setup as Troika [15] and CSP [41]: images are processed with the same resizing and cropping pipeline, and Adam is used as the optimizer for all datasets. For *FlowComposer*, we utilize AdamW [35] as the optimizer for both primitive flows and the composer.

Flow Matching Networks. As introduced in the main paper Sec. 5.1, We employ a lightweight architecture proposed in MAR [27] as flow matching network, implemented as a deep residual MLP with timestep conditioning. Concretely,

the input feature $x \in \mathbb{R}^D$ (CLIP feature of dimension D) is fed into a stack of 24 ResBlocks with adaptive LayerNorm (adaLN) modulation, where timestep embeddings from a small MLP (*TimestepEmbedder*) control per-channel shift, scale, and gating, and each block uses SiLU activations.

Composer Networks. We implement the *Composer* as a lightweight residual MLP that takes the attribute and object velocities $v_a, v_o \in \mathbb{R}^D$ as input, and processes them with LayerNorm, GELU activations, and a small stack of residual MLP blocks before projecting back to \mathbb{R}^D . We report the details of the model parameters in Tab. 7.

Table 7. Model size and computational cost of our networks.

Network	# Params (M)↓	GFLOPs↓
FM	74.06	0.07
Composer	25.97	0.03

8. Remained Feature Entanglement Analysis

8.1. Leakage Analysis

To further support our argument about *Remained Feature Entanglement*, we quantitatively probe the amount of cross-branch “leakage” in the multi-path baseline Troika [15]. Our hypothesis is that, under perfect disentanglement, the attribute branch should encode only attribute-related information and be essentially uninformative for object prediction (and vice versa). In that case, using attribute features to classify objects (or object features to classify attributes) should yield accuracies close to random chance. To test this, we extract the attribute, object, and composition features from Troika [15] on the test sets and use each branch to predict both attribute and object labels with the same CLIP-style cosine classifier aligned with Troika’s inference. We then measure the resulting attribute and object accuracies for all three branches on all three datasets, and report the results in Tab. 8.

In Tab. 8 we report *class-balanced accuracy* (per-class average). The first row (Random) is a chance baseline with randomly generated predictions. The second row (*Attr Branch*) uses the *attribute* image features to classify both attributes and objects via the same CLIP-style cosine classifier; the third row (*Obj Branch*) does the symmetric test with *object* features; the fourth row (*Comp Branch*) uses the *composition* features. Clear leakage emerges: using attribute features to predict *objects* is far above chance (MIT: **3.87** vs. 0.47, UT: **14.9** vs. 8.14, C-GQA: **2.36** vs. 0.05).

Conversely, using object features to predict *attributes* also surpasses chance (MIT: **6.3** vs. 1.13, UT: **7.69** vs. 5.74, C-GQA: **2.12** vs. 0.25). Moreover, composition features are strongly predictive for both primitives (*e.g.*, object accuracy: MIT **51.3**, UT **58.9**, C-GQA **39.8**), indicating substantial cross-branch carry-over. These findings are inconsistent with perfect disentanglement and quantitatively support our claim of *remained feature entanglement*.

Table 8. Comparison between random prediction and predictions from *Attribute*, *Object* and *Composition* branches on class-balanced accuracy (*Acc*) for attributes and objects.

Acc(%)	MIT-States		UT-Zappos		C-GQA	
	Attr	Obj	Attr	Obj	Attr	Obj
Random	1.13	0.47	5.74	8.14	0.25	0.05
Attr Branch	26.3	3.87	22.3	14.9	3.64	2.36
Obj Branch	6.3	45.2	7.69	63.2	2.12	17.3
Comp Branch	21.3	51.3	21.6	58.9	9.72	39.8

8.2. Disentanglement Analysis

We further refine our analysis by examining the role of the visual disentangler itself. In our initial cross-branch probe, we observe that on certain datasets the attribute and object branches can even become less predictive when the disentangler suppresses information too aggressively, suggesting that disentanglement may sometimes remove useful cues together with entangled ones. To better understand whether the disentangler remains beneficial overall, we conduct an additional controlled study: using the same backbone and training protocol, in Tab. 9, we compare (i) **w/ Disentangler**, the standard multi-path baseline [15], against (ii) **w/o Disentangler**, a variant in which we remove the disentangler.

Across all datasets, removing the disentangler leads to clear drops in HM and AUC, indicating that feature disentanglement, although imperfect and not strictly factor-pure, still provides meaningful structural benefits for compositional generalization.

In summary, the cross-branch “leakage” accuracies remain far above random under both settings, reinforcing our central observation that *perfect* attribute–object separation is difficult to achieve in practice. This aligns with the motivation of our main paper: rather than pursuing an idealized, fully factorized representation, we embrace the remaining entanglement and turn it into a resource. Leakage-Guided Augmentation is therefore designed not to eliminate leakage, but to harness the surviving cross-factor signals as additional supervision, reflecting the philosophy that residual correlations, when properly guided, can be leveraged rather than suppressed.

Table 9. Comparison between Troika and Troika without disentangler in MIT-States [17], UT-Zappos [52] and C-GQA [39] on HM and AUC under the closed-world setting.

Disentangler	MIT-States		UT-Zappos		C-GQA	
	HM	AUC	HM	AUC	HM	AUC
w	39.2	22.1	55.4	41.8	29.7	12.5
w/o	36.8	20.4	51.4	37.5	28.0	11.2

9. Additional Analysis

9.1. Additional Component Analysis

We provide additional component analysis to quantify the contribution of each module: *Primitive Flows (Flows)*, *Composer*, and *Leakage-Guided Augmentation (LG-Aug)* under the *open-world* setting. As shown in Tab. 10, we report results on MIT-States [17], UT-Zappos [52], and C-GQA [39], comparing against the Troika [15] baseline. Starting from the baseline, we incrementally add our components and make four observations. **First**, introducing *Primitive Flows* (Row (1)) delivers a consistent boost, especially on seen accuracy, indicating that explicit transport toward textual endpoints helps beyond token-level composition. **Second**, adding *Leakage-Guided Augmentation* on top of Flows (Row (2)) further improves robustness on unseen pairs, yielding higher HM and AUC by leveraging residual cross-branch cues. **Third**, alternatively replacing LG-Aug with the *Composer* (Flows+Composer, Row (3)) also stabilizes recognition by providing an explicit combination rule in the embedding space, improving HM and AUC over Flows alone. **Fourth**, combining all components (**Ours**) achieves the best performance across all datasets and metrics, demonstrating that explicit velocity composition and leakage-guided supervision are complementary to flow learning in the open-world regime.

9.2. Computational Costs

Tab. 11 reports the inference-time comparison between two baselines (CSP [41] and Troika [15]) and our *Flow-Composer*. We report the average latency (ms) per image over the entire test set. Our method increases latency only slightly (*e.g.*, from 17.6 to 19.2 ms per image on MIT-States [17], 11.0 to 12.7 ms per image on UT-Zappos [52], and 69.8 to 74.4 ms per image on C-GQA [39] for Troika [15]). This modest cost stems from our one-step transport scheme and lightweight Composer, indicating that the performance gains come with negligible computation.

9.3. Composition Stepsize Analysis

We introduce the hyperparameter stepsize h of the one-step composition in Sec. 4.2. As shown in the main paper Tab. 3, we evaluate $h \in \{0.1, 0.5, 1.0\}$ on MIT-States [17] and UT-Zappos [52] under the closed-world setting. The optimal h

Table 10. Ablations. The results regarding the different components in our *FlowComposer* on MIT-States [17], UT-Zappos [52] and C-GQA [39] under the open-world setting.

	<i>Flows</i> (§ 4.1)	<i>Composer</i> (§ 4.2)	<i>LG-Aug</i> (§ 4.3)	MIT-States [17]				UT-Zappos [52]				C-GQA [39]			
				Seen	Unseen	HM	AUC	Seen	Unseen	HM	AUC	Seen	Unseen	HM	AUC
Baseline	✗	✗	✗	50.3	17.5	19.0	6.8	65.8	61.0	46.6	32.7	40.8	8.6	11.7	2.9
(1)	✓	✗	✗	50.1	18.0	19.6	7.0	68.5	60.8	49.3	33.8	41.2	9.0	12.0	3.2
(2)	✓	✗	✓	49.7	18.9	20.2	7.3	69.1	61.5	50.1	34.7	42.2	10.0	12.3	3.3
(3)	✓	✓	✗	49.6	18.8	20.0	7.2	69.8	61.1	50.7	34.9	41.9	10.3	12.2	3.2
Ours	✓	✓	✓	50.4	19.0	20.3	7.5	70.1	61.2	51.0	35.5	43.5	10.2	12.6	3.5

Table 11. Inference time (ms/image) comparison between two baselines and ours.

Method	MIT-States	UT-Zappos	C-GQA
CSP	6.6	10.3	20.2
+ Ours	9.3	12.5	24.6
Troika	17.6	11.0	69.8
+ Ours	19.2	12.7	74.4

differs across datasets: UT-Zappos [52] favors a larger step ($h=1.0$), whereas MIT-States [17] prefers smaller steps. We attribute this to dataset-specific composition geometry: UT-Zappos contains fewer, more separated compositions, where a longer step moves features closer to their text targets; in contrast, the denser composition spaces of MIT-States make large steps prone to overshooting and error accumulation. Accordingly, we adopt dataset-specific choices of h in all experiments.

Here, we provide an additional ablation study on C-GQA [39]. As shown in Tab. 12, the trend on C-GQA [39] mirrors the behavior observed in MIT-States [17] and UT-Zappos [52]. A smaller composition stepsize ($h=0.1$) yields the best performance across all four metrics on both the validation and test sets. Larger stepsizes ($h=0.5$ and $h=1.0$) consistently reduce HM and AUC, indicating that overly long updates tend to overshoot the target direction in C-GQA’s dense composition space. The close alignment between validation and test results further confirms that the stepsize sensitivity is stable and not due to overfitting or evaluation noise. This provides additional support that different datasets exhibit distinct composition geometries, and that adopting dataset-specific stepsizes leads to more reliable one-step transport.

Table 12. Results regarding stepsize h (§ 4.2) on the validation and test set under the closed-world setting for C-GQA [39].

h	Validation				Test			
	S	U	H	A	S	U	H	A
0.1	44.6	40.6	32.9	15.5	44.8	40.7	34.0	15.9
0.5	44.6	39.9	32.6	15.2	43.8	40.0	32.9	15.1
1.0	42.0	36.7	29.8	13.0	40.3	36.9	29.7	12.7

10. Stability Analysis

Following standard practice [15, 41], we further evaluate the stability of our method over 5 random seeds. Tab. 13 reports the mean and standard deviation across five independent runs on all three benchmarks. The variances remain consistently small, and the performance gains over both baselines persist under this multi-run setting. Notably, even on the challenging C-GQA dataset, *FlowComposer* delivers stable and reproducible improvements. These results demonstrate that *FlowComposer* is not only effective but also robust to different initializations.

11. Semantic Analysis of Composer

To better understand the behavior of our *Composer* and examine whether the predicted combination coefficients carry semantic meaning, we visualize the predicted attribute and object weights (\hat{a}, \hat{b}) for correctly classified samples across the three datasets using the *FlowComposer* based on Troika [15]. Recall that \hat{a} and \hat{b} correspond to the contributions of the attribute and object velocities when composing the final composition velocity. Importantly, our intention is not to enforce that the ground-truth composition velocity must lie exactly in the span of the primitive velocities, $\text{span}\{v_{\text{attr}}, v_{\text{obj}}\}$. Instead, the *Composer* aims to predict an approximate combination that produces a composition velocity pointing toward the desired semantic direction. As shown in Fig. 5, the learned coefficients indeed correlate with the visual prominence of attribute and object cues, demonstrating that the *Composer* adapts its weighting based on the evidence present in the image.

Across the visualizations, we observe clear and consistent semantic tendencies. When an attribute is visually salient, such as distinctive material patterns, strong color cues, or highly recognizable texture changes, the predicted attribute coefficient \hat{a} increases. In contrast, when the attribute is abstract, weakly expressed, or visually ambiguous, the *Composer* assigns a smaller value to \hat{a} , relying more heavily on the object velocity. Similarly, when the object identity is visually clear and structurally well preserved, the object coefficient \hat{b} becomes dominant; however, if the object shape is partially occluded, deformed,

Table 13. Performance on MIT-States [17], UT-Zappos [52], and C-GQA [39], averaged over 5 random seeds with corresponding standard deviations. * marks results taken from the respective original publications.

Method	MIT-States [17]				UT-Zappos [52]				C-GQA [39]			
	Seen	Unseen	HM	AUC	Seen	Unseen	HM	AUC	Seen	Unseen	HM	AUC
CSP* [41][ICLR23]	46.6 \pm 0.1	49.9 \pm 0.1	36.3 \pm 0.1	19.4 \pm 0.1	64.2 \pm 0.7	66.2 \pm 1.2	46.6 \pm 1.2	33.0 \pm 1.3	28.8 \pm 0.1	26.8 \pm 0.1	20.5 \pm 0.1	6.2 \pm 0.0
+FlowComposer	48.4 \pm 0.2	50.4 \pm 0.1	37.8 \pm 0.2	20.7 \pm 0.1	66.9 \pm 0.4	68.0 \pm 0.7	51.4 \pm 0.7	38.2 \pm 0.8	29.0 \pm 0.1	31.0 \pm 0.2	23.1 \pm 0.2	7.8 \pm 0.2
Troika* [15][CVPR24]	49.0 \pm 0.4	53.0 \pm 0.2	39.3 \pm 0.2	22.1 \pm 0.1	66.8 \pm 1.1	73.8 \pm 0.6	54.6 \pm 0.5	41.7 \pm 0.7	41.0 \pm 0.2	35.7 \pm 0.3	29.7 \pm 0.2	12.4 \pm 0.1
+FlowComposer	51.7 \pm 0.3	53.1 \pm 0.1	40.2 \pm 0.1	23.4 \pm 0.1	71.5 \pm 0.6	75.0 \pm 0.3	58.8 \pm 0.4	46.7 \pm 0.3	44.8 \pm 0.1	40.6 \pm 0.1	34.1 \pm 0.1	15.9 \pm 0.1

or visually degraded, the Composer reduces \hat{b} and compensates through attribute evidence. These trends appear consistently across MIT-States [17], UT-Zappos [52], and C-GQA [39], despite the substantial differences in attribute style, object granularity, and visual complexity among the datasets. For example, in MIT-States [17], attributes such as `sliced` or `squished` exhibit strong, localized visual patterns, leading to larger \hat{a} , whereas abstract attributes like `unripe`, `clean` or `dark` produce much smaller coefficients due to their weak visual expression. Similarly, in C-GQA [39], samples with vivid attribute cues (e.g., `blue coat`, `brown dog` or `painted wall`) yield higher \hat{a} , while cases where the attribute is subtle or occluded (e.g., `blue waterblack bicycle`, or `Fried Dough`) shift the weighting toward the object, resulting in larger \hat{b} . For the UT-Zappos [52] dataset, the attribute typically describes material or surface appearance (e.g., `leather`, `satin`, `canvas`), which is prominently expressed on the shoe surface, while the object denotes the shoe type, whose structural cues are often less visually distinctive. As a result, the attribute coefficient \hat{a} consistently dominates across UT-Zappos samples, reflecting the stronger visual salience of material-based attributes.

The sample-level behaviors in Fig. 5 further highlight the interpretability of the predicted coefficients. When attribute cues are strong or highly distinctive, the Composer increases the corresponding attribute weight, whereas objects with vivid, easily recognizable visual characteristics naturally lead to larger object coefficients. For example, in the two `blue coat` samples from C-GQA [39], the first image exhibits a much more prominent blue coloration, leading to a larger attribute coefficient, whereas in the second image the coat shape is clearly visible but the blue cue is relatively weak, resulting in a higher object coefficient \hat{b} . Similarly, for the two `moldy tomato` samples from MIT-States [17], the upper image contains more pronounced moldy regions and multiple clearly visible tomatoes, which yields larger values for both the attribute and the object coefficients compared to the lower sample, where the mold is less salient and fewer tomatoes are present.

These observations collectively reinforce the core motivation behind our *Composer*: different composites and even different samples of the same composite exhibit vary-

ing visual contributions from the attribute and the object, so a fixed weighting scheme (as used in prior multi-branch methods such as Troika [15]) cannot adequately capture such diversity. In contrast, our learned coefficients provide sample-specific balancing of primitive velocities, allowing the model to adapt its reliance on attribute or object information according to their respective visual strengths. This semantic analysis therefore supports our design choice of learning explicit, data-dependent combination coefficients and demonstrates that the *Composer* produces weights that align with human-interpretable visual cues rather than applying uniform or heuristic mixing rules.

12. Social Impacts

This paper presents a feasible approach to compositional zero-shot learning, enabling models to recognize novel attribute-object compositions from known primitives, which may potentially benefit a variety of applications such as retrieval, assistive perception, or visual reasoning in open-world environments. However, there remains a potential risk associated with the reliance on pretrained vision-language models and benchmark datasets. In particular, our method may inherit and amplify dataset biases—such as skewed attribute distributions or culturally sensitive descriptors—which can propagate through the compositional mechanism. Such amplified biases may in turn lead to incorrect or inappropriate composition predictions in high-stakes scenarios, where misidentifying attributes or objects could result in harmful downstream decisions. Additionally, to mitigate potential negative social impacts, the development of rigorous bias-auditing tools, transparent evaluation practices, and responsible deployment protocols is crucial to ensure that such models do not propagate harmful biases or influence high-stakes decisions without proper safeguards.

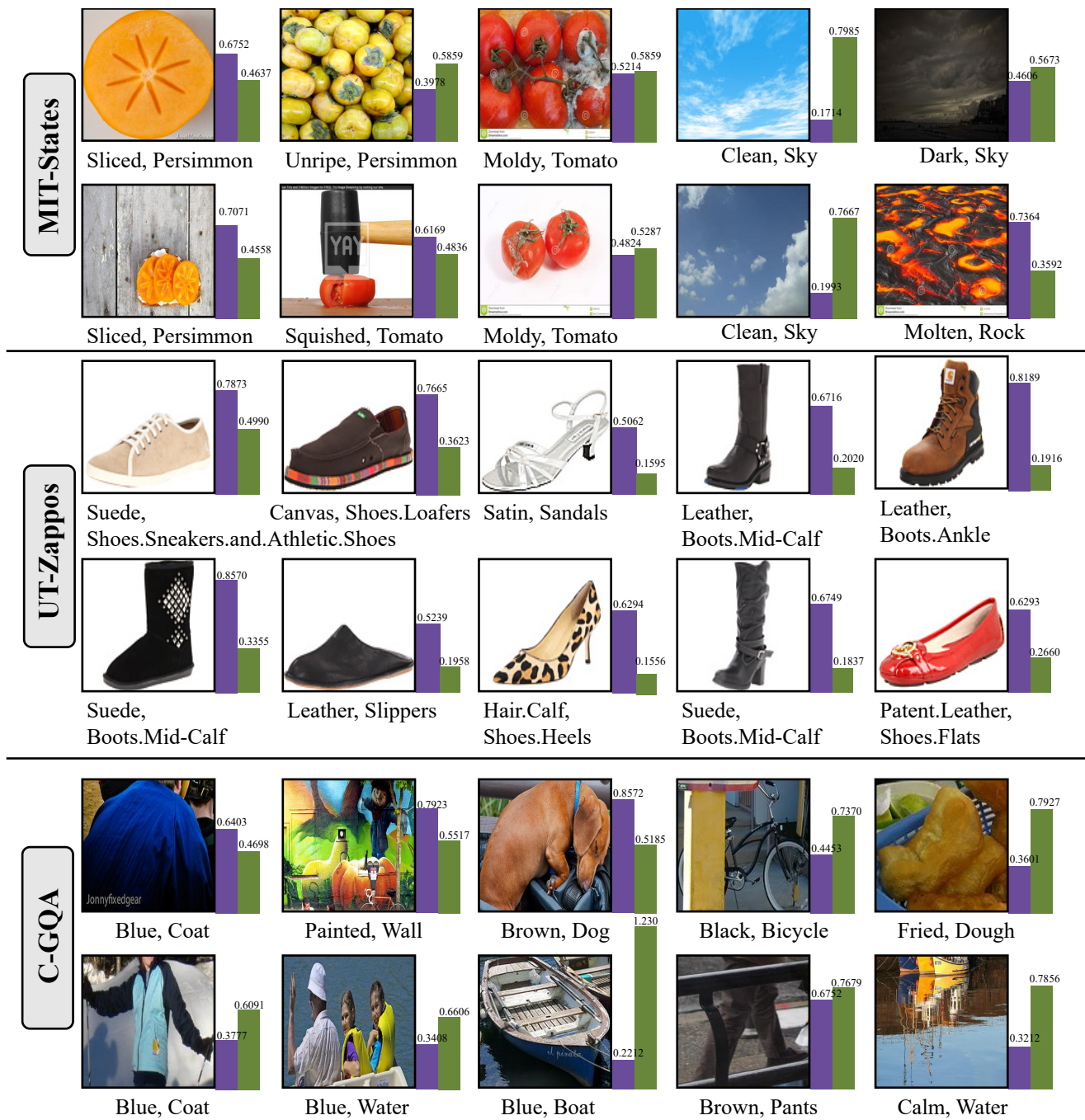


Figure 5. The purple bar \hat{a} denotes the value of \hat{a} and the green bar \hat{b} denotes the value of \hat{b} , which are the coefficients for attribute and object velocities respectively.